Critical behavior in the itinerant ferromagnet $AsNCr_3$ with tetragonal-antiperovskite structure

Shuai Lin,[1] Hongyan Lv,[1] Jianchao Lin,[1] Yanan Huang,[1] Lei Zhang,[2] Wenhai Song,[1] Peng Tong,[1,*] Wenjian Lu,[1] and Yuping Sun[1,2,3,†]

[1]*Key Laboratory of Materials Physics, Institute of Solid State Physics, Chinese Academy of Sciences, Hefei 230031, People's Republic of China*

[2]*High Magnetic Field Laboratory, Chinese Academy of Sciences, Hefei 230031, People's Republic of China*

[3]*Collaborative Innovation Center of Advanced Microstructures, Nanjing University, Nanjing 210093, People's Republic of China*

(Received 8 August 2017; revised manuscript received 27 March 2018; published 9 July 2018)

Herein, we have systematically reported the synthesis, structure, magnetism, and electrical/thermal transport properties of $AsNCr_3$. Tetragonal-antiperovskite metallic $AsNCr_3$ exhibits a second-order ferromagnetic (FM)-paramagnetic (PM) transition around 243 K, where the resistivity and specific heat also show a related change. Based on the obtained parameters from basic physical properties, the nature of weak electron-electron correlation was confirmed by both the Kadowaki-Woods ratio and Wilson ratio. Moreover, the value of the Rhodes-Wolfarth ratio (1.312) is larger than 1, suggesting an itinerant ferromagnetism in $AsNCr_3$. To further clarify the magnetic interaction of the $AsNCr_3$ system, the study of critical behavior around the FM-PM transition has been performed. The critical exponents (β, γ, and δ) of $AsNCr_3$ obtained from different methods are very close to the theoretical values of the mean-field model ($\beta = 0.5$, $\gamma = 1.0$, and $\delta = 3.0$), indicating the existence of a long-range FM interaction. Besides, the exchange interaction distance $J(r) \sim r^{-4.3}$ for $AsNCr_3$ decreases more slowly than that of mean-field model $J(r) \sim r^{-4.5}$, further confirming the long-range magnetic coupling in our system. The strong hybridization between Cr-3d and N-2p states as well as between Cr-3d and As-4p states confirmed by our theoretical calculations results in the itinerant characterization of carriers and the long-range FM interaction in tetragonal-antiperovskite $AsNCr_3$.

DOI: 10.1103/PhysRevB.98.014412

I. INTRODUCTION

Recently, the antiperovskite compounds with a formula AXM_3 (A = Ga, Al, Sn, Zn, Cu, In, Ge, As, Sb, etc.; X = C, N; M = Cr, Mn, Fe, Ni, etc.) have been studied extensively owing to their interesting properties, such as superconductivity [1], zero temperature resistivity coefficient [2–4], giant magnetoresistance effect [5,6], giant barocaloric effect [7], phase separation [8], negative thermal expansion [9], magnetocaloric effect [10], spin-glass behavior [11–14], and magnetostriction [15]. In general, the symmetry of crystal structure is cubic with the space group Pm-3m (No. 221) for most of antiperovskite compounds AXM_3 [16]. However, the tetragonal symmetry, although rare in antiperovskite compounds, was observed in $GeNFe_3$ [17,18], $CuNMn_3$ (below 149 K) [9,19], $SbNMn_3$ [20], $GeNCr_3$ [21], and $AsNCr_3$ [16,22–24]. Some of these tetragonal-antiperovskite compounds have been investigated and many interesting properties were observed. For instance, $GeNFe_3$ shows a spin-glass behavior and anomalous Hall effect [17,18], chemically doped $CuNMn_3$ exhibits excellent negative thermal expansion and abnormal ferromagnetic (FM) critical behavior [9,19], $SbNMn_3$ undergoes a giant magnetostriction [20], $GeNCr_3$ shows a first-order antiferromagnetic (AFM)-paramagnetic (PM) transition with large thermal hysteresis [21]. $AsNCr_3$ as a tetragonal-antiperovskite structure nitride was reported in 1968, but its physical properties were rarely reported up to now [22,23]. Thus, it is necessary and interesting to investigate the physical properties of tetragonal-antiperovskite $AsNCr_3$.

In this paper, we successfully synthesized $AsNCr_3$ and systematically reported its basic physical properties, such as magnetism, electrical transport, and specific heat. A second-order FM-PM transition was observed around 243 K. Based on the obtained basic physical data, we got the Kadowaki-Woods ratio (R_{KW}), Wilson ratio (R_W), and the Rhodes-Wolfarth ratio (RWR), confirming the weak electron-electron correlation and itinerant ferromagnetism in $AsNCr_3$. Detailed critical behavior is performed around the FM-PM phase transition. The obtained critical exponents (β, γ, and δ) are close to the values of the mean-field model and the exchange-interaction distance is obtained as $J(r) \sim r^{-4.3}$, confirming the existence of a long-range FM interaction in $AsNCr_3$. Our theoretical calculations show a strong hybridization between Cr-3d and N-2p states as well as between Cr-3d and As-4p states in tetragonal-antiperovskite $AsNCr_3$, resulting in the itinerant characterization of carriers and the long-range FM interaction.

II. EXPERIMENT AND CALCULATION DETAILS

Polycrystalline sample of $AsNCr_3$ was prepared by the conventional solid-state reaction. Powders of As (3N, Alfa Aesar), Cr (4N, Alfa Aesar), and CrN (3N, Alfa Aesar) were mixed in the desired proportions, pressed into pellets (at a pressure of 25 MPa, diameter is 12 mm, thickness is 2–3 mm),

*tongpeng@issp.ac.cn
†ypsun@issp.ac.cn

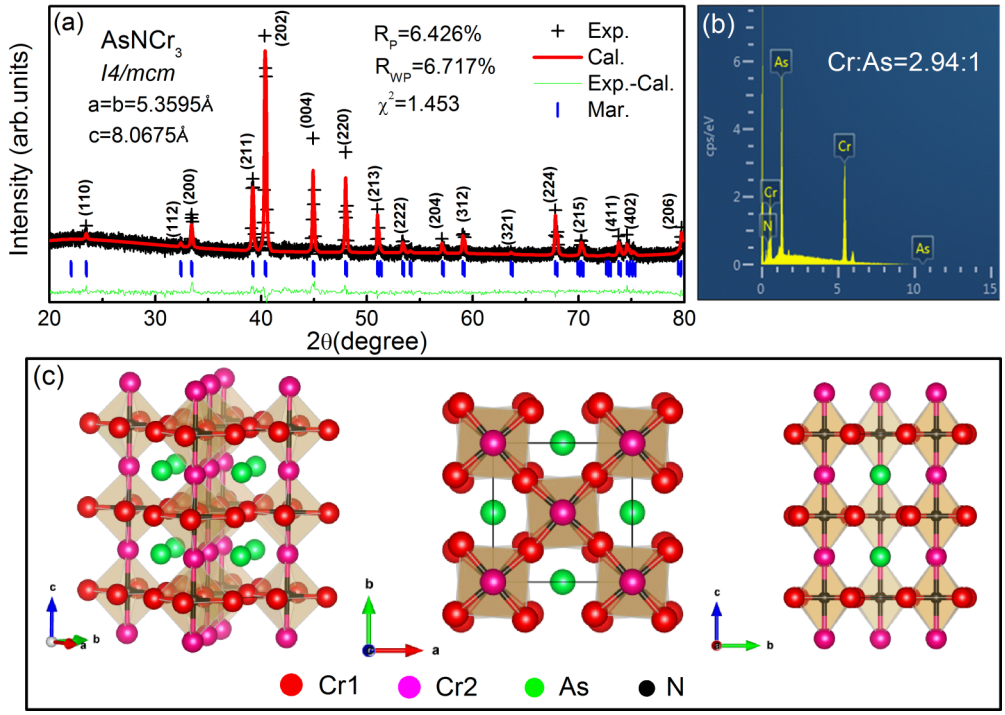

FIG. 1. (a) Rietveld refined powder XRD patterns at room temperature for $AsNCr_3$. The vertical marks (blue line) stand for the position of Bragg peaks, and the solid line (green line) at the bottom correspond to the difference between experimental and calculated intensities. (b) EDS information on $AsNCr_3$. (c) Sketches of crystal structure with different directions for $AsNCr_3$.

sealed in evacuated quartz tubes ($<10^{-3}$ Pa), and then annealed at 1073 K for about 5–7 d. After quenching the tubes to room temperature, the products were pulverized, mixed, pressed into pellets, and annealed again at 1173 K for about more than a week to obtain a good-quality sample. X-ray powder diffraction (XRD) was performed using a Philips X′pert PRO x-ray diffractometer with Cu K_α radiation ($\lambda = 0.15406$ nm) from 300 to 35 K. The Rietveld refinement of XRD data was carried out by using the RIETICA software. The compositions of our sample were determined by electron-dispersive spectrometer (EDS). Magnetic measurements were carried out on a Quantum Design superconducting quantum interference device magnetometer (SQUID-5T). The electrical/thermal transport properties were characterized on a Quantum Design physical property measurement system (PPMS-9T). The electrical transport measurements were performed by a four-probe method to eliminate contact resistance. The measurement of specific heat was carried out by a heat-pulse relaxation method on PPMS-9T. Differential thermal scanning (DSC) was measured by using a Diamond differential scanning calorimeter between 230 and 300 K.

First-principles calculations based on density-functional theory were performed by using the projector-augmented wave method as implemented in the Vienna *Ab initio* Simulation Package (VASP) [25,26]. The exchange-correlation potential was in the form of Perdew-Burke-Ernzerhof with generalized gradient approximation. In the self-consistent calculations, the Brillouin zone of primitive cell was sampled with a $12\times12\times12$ Monkhorst-Pack k-point mesh. For the density of states (DOS) calculations, a denser $25\times25\times25$ mesh of k points was used. The energy cutoff of the plane-wave basis was set to be 500 eV. Both the lattice parameters and atomic positions were fully relaxed until the force acting on each atom became less than 0.01 eV/Å.

III. RESULTS AND DISCUSSION

A. Characterization of basic physical property

Figure 1(a) shows the Rietveld refinement of room-temperature powder XRD patterns of $AsNCr_3$. All the diffraction peaks could be indexed to the corresponding structure and space group ($I4/mcm$, No. 140). There are no obvious impurity peaks. The related fitting parameters (such as χ^2, R_p, and R_{wp}) are quite small as presented in Fig. 1(a), suggesting that our sample is of high quality. The refined lattice constants are $a = b = 5.3595(3)$ Å and $c = 8.0675(2)$ Å, which match well with the previously reported values ($a = b = 5.36$ Å and $c = 8.066$ Å) [22,24]. All the parameters of the Rietveld refinement were summarized in Table I. Figure 1(b) displays the EDS results of $AsNCr_3$, and the value of As : Cr = 1 : 2.94, which is much close to the stoichiometric ratio of 1:3 within the experimental error. Here, it is necessary to point out that the N element is too light to be accurately determined by EDS. In fact, the N element is approaching to nominal composition, which will be discussed later. According to the above fitting parameters, we obtain the sketch map of crystal structure for $AsNCr_3$ as shown in Fig. 1(c). The twisting of the linked Cr_6N octahedra along the c axis can be easily found in the middle and right panels of Fig. 1(c), which is consistent with the previous report [23].

Figure 2(a) presents the temperature-dependent magnetization $M(T)$ under zero-field-cooled (ZFC), field-cooled cooling (FCC), and field-cooled warming (FCW) processes,

TABLE I. Crystallographic information and refinement parameters obtained from the Rietveld refinement of powder XRD data of $AsNCr_3$.

Item	$AsNCr_3$			
Crystal system	Tetragonal			
Space group	$I4/mcm$			
Lattice constants (Å)	$a = b = 5.3595$ (This work) ($a = b = 5.36$) (Ref. [22]) $c = 8.0675$ (This work) ($c = 8.066$) (Ref. [22])			
Cell volume ($Å^3$)	231.73			
Formula units	4			
$\alpha/\beta/\gamma$ (°)	90/90/90			
R_P (%)	6.426			
R_{WP} (%)	6.717			
χ^2	1.453			
$AsNCr_3$	Wyckoff symbol	x	y	z
Cr1	8*h*	0.185	0.685	0
Cr2	4*a*	0	0	0.25
As	4*b*	0	0.5	0.25
N	4*c*	0	0	0

the differentiation of $M(T)$ (ZFC), and inverse susceptibility $\chi^{-1}(T)$ (ZFC) curves of $AsNCr_3$ at a magnetic field of 1 kOe between 5 and 300 K. As shown in $M(T)$ curve of Fig. 2(a), a magnetic transition occurs around 243 K, which is similar to the previous report [24]. Around magnetic phase transition, there is no obvious thermal hysteresis between $M_{FCC}(T)$ and $M_{FCW}(T)$ curves, indicating a second-order phase transition. Figure 2(b) shows the isothermal $M(H)$ curves for $AsNCr_3$ at 5 and 300 K. Especially, the coercive force is only 24 Oe and the saturation magnetization (μ_S) is about 4.35 emu/g (0.0636 μ_B/Cr) at 5 K. The room-temperature PM state is observed from the linear $M(H)$ curve at 300 K. In order to get more information about the magnetism of $AsNCr_3$, we made a well-fitted $\chi^{-1}(T)$ curve above 250 K by using the modified Curie-Weiss law [27]:

$$\chi(T)^{-1} = \left(\frac{C}{T-\theta} + \chi_0\right)^{-1}, \tag{1}$$

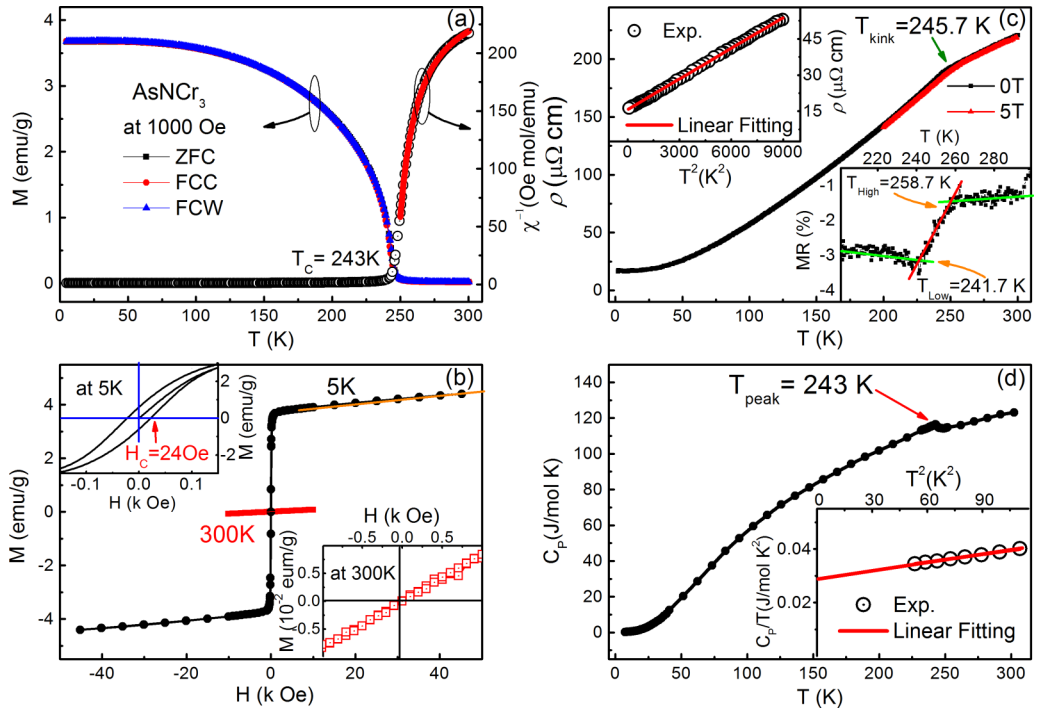

FIG. 2. (a) Temperature-dependent magnetization $M(T)$ curves under ZFC and FC processes and inverse susceptibility $\chi^{-1}(T)$ (ZFC) curves of $AsNCr_3$ at a magnetic field of 1 kOe between 5 and 300 K. (b) $M(H)$ curves at 5 and 300 K. The left and right inset show the enlargement of $M(H)$ curve at 5 and 300 K with low magnetic fields. (c) Temperature dependence of resistivity $\rho(T)$ at 0 and 5 T for $AsNCr_3$. The left inset presents the lower-T $\rho(T)$ data plotted as $\rho(T)$ vs T^2. The right inset reveals the MR effect around FM-PM transition. (d) Temperature-dependent heat capacity $C_P(T)$ at zero magnetic field between 5 and 300 K for $AsNCr_3$. Inset displays the plot of $C_P(T)/T$ vs T^2 below 10 K and the solid line represents the linear fitting results according to Eq. (3).

TABLE II. Parameters of magnetism, electrical transport, and low-temperature specific heat in $AsNCr_3$.

	$AsNCr_3$
χ_0 (10^{-4} emu/mol)	3.82(1)
C (emu K/mol)	0.065(1)
θ (K)	247.2(1)
$\mu_{\rm eff}$ (μ_B/Cr)	0.417(2)
μ_S (μ_B/Cr)	0.0636
ρ_0 ($\mu\Omega$ cm)	15.8(1)
A (10^{-3} $\mu\Omega$ cm/K^2)	4.23(1)
RRR ($\rho_{300\,\rm K}/\rho_{2\,\rm K}$)	15
γ (mJ/mol K^2)	29.3(1)
β (mJ/mol K^4)	0.096(2)
δ (10^{-6} mJ/mol K^6)	3.12(5)
$\Theta_{\rm D}$ (K)	466.1(3)

where C is the Curie constant, θ stands for the Weiss temperature, and χ_0 is a temperature-independent term, namely, the Pauli paramagnetic term. Correspondingly, we get the values of parameters as follows: $C = 0.065(1)$ emu K/mol, $\theta = 247.2(3)$ K, $\chi_0 = 3.82(1)\times10^{-3}$ emu/mol Oe. The positive Weiss temperature indicates the FM exchange interaction in this system. The effective magnetic moment per Cr atom ($\mu_{\rm eff}$) is estimated as $0.417(2)\,\mu_B$/Cr from the relationship $\mu_{\rm eff} = 2.83(C/\eta)^{0.5}\,\mu_B$ (where C is the Curie constant and η is the number of magnetic atoms in a unit cell and equals to 3 in our sample) [28]. The estimated $\mu_{\rm eff}$ ($0.417\,\mu_B$/Cr) is much smaller than the local magnetic moment of Cr ($2.5\,\mu_B$/Cr) [29], suggesting that the $3d$ electrons of Cr in $AsNCr_3$ are mainly itinerant. Given the values of $\mu_{\rm eff}$ and μ_S, the Rhodes-Wolfarth ratio can be calculated [30]. According to Rhodes and Wolfarth, RWR $= \mu_C/\mu_S$, where μ_C is related to the number of moving carriers and can be obtained from $\mu_{\rm eff}^2 = (\mu_C + 2)\,\mu_C$. If $\mu_C = \mu_S$, i.e., RWR $= 1$, the magnetism is localized, whereas RWR > 1 suggests the existence of itinerant ferromagnetism [29,30]. Here, in our case, the obtained RWR is 1.312(1), indicating an itinerant ferromagnetism in our system.

Figure 2(c) displays the temperature dependence of resistivity $\rho(T)$ for $AsNCr_3$ at zero magnetic field and 5 T between 2 and 300 K. Apparently, there exists a kink around 245.7 K, and the magnitude of $\rho(T)$ increases basically with increasing temperature, indicating a good metallic behavior. Negative magnetoresistance MR $= [\rho(5\rm T) - \rho(0\rm T)]/\rho(0\rm T)$ is observed around FM-PM transition, which can be found in the right inset of Fig. 2(c). Obviously, the value of MR undergoes a sharp change between 258.7 and 241.7 K, among which the FM-PM transition happens. As shown in left inset of Fig. 2(c), the low-temperature resistivity is well fitted by the formula [28]

$$\rho = \rho_0 + AT^2, \tag{2}$$

where ρ_0 and A represent the residual resistivity and T^2-term coefficient of the resistivity, respectively. This suggests a Fermi liquid behavior at low temperatures for $AsNCr_3$. Correspondingly, the fitting values of parameters $\rho_0 = 15.8(1)\,\mu\Omega$ cm and $A = 0.00423(1)\,\mu\Omega\,\rm cm/K^2$ are obtained. The low-temperature residual resistivity ρ_0 and the residual resistivity ratio (RRR), defined as RRR $= \rho(300\,\rm K)/\rho(2\,\rm K)$, are measures of sample quality such as in metals and alloys

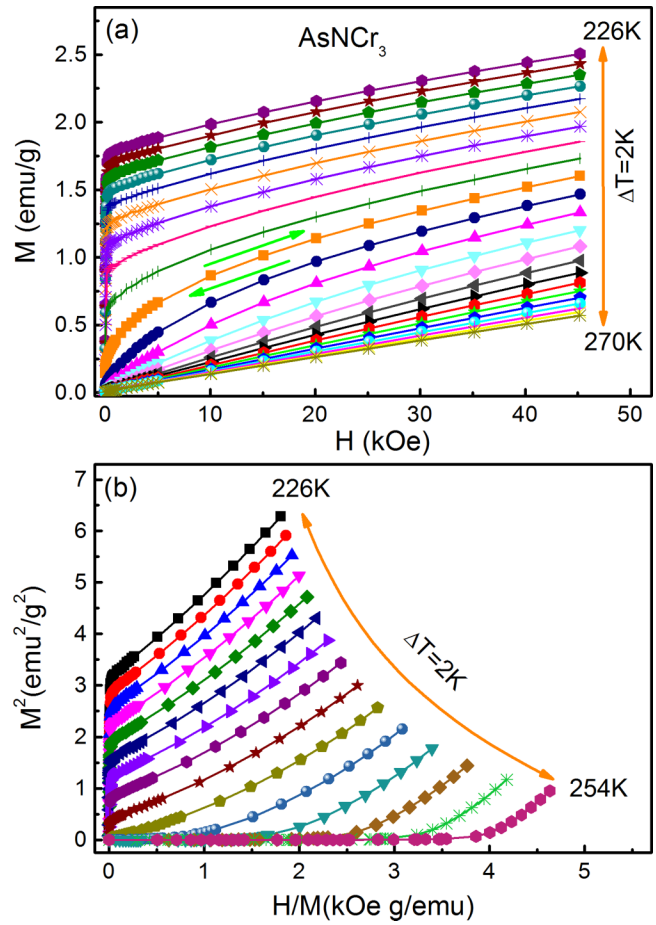

FIG. 3. (a) The initial isothermal magnetization around T_C. (b) The Arrott plot of H/M vs M^2.

[31]. High-ρ_0 and small-RRR values suggest sizable scattering from impurities, vacancies, or other defects [31]. In contrast, the small ρ_0 ($\sim$15.8 $\mu\Omega$ cm) and relatively large RRR ($\sim$15) indicate a relatively good quality of our sample.

Figure 2(d) plots the specific heat $C_P(T)$ curves between 5 and 300 K for $AsNCr_3$. The specific heat of $AsNCr_3$ at 300 K is 123.2 J/mol K, which is very close to the classical Dulong-Petit value $C_{\rm V} = 3nR = 124.7$ J/mol K for the specific heat due to acoustic lattice vibrations [32], where n is the number of atom per formula unit (here, $n = 5$ for $AsNCr_3$). This confirms that the compositions of our sample is very close to the nominal composition, that is to say, N defect is very small for our sample. Apparently, there is a peak around FM-PM transition. However, this peak is not as sharp as the "λ" peak, suggesting a second-order magnetic phase transition [29]. Moreover, we also measured the DSC between 300 and 230 K (see the Fig. S1 of Supplemental Material) [33], but neither an exothermic nor endothermic peak was detected around FM-PM transition, further confirming a second-order phase transition. The inset of Fig. 2(d) shows the low-temperature (below 10 K) specific heat $C_{\rm P}(T)$ of $AsNCr_3$ plotted as $C_{\rm P}(T)/T$ vs T^2, which can be well expressed by the following equation [28]:

$$C_P(T) = \gamma T + \beta T^3 + \delta T^5, \tag{3}$$

where γ is the electron specific heat coefficient (Sommerfeld constant), β stands for phonon specific heat coefficient,

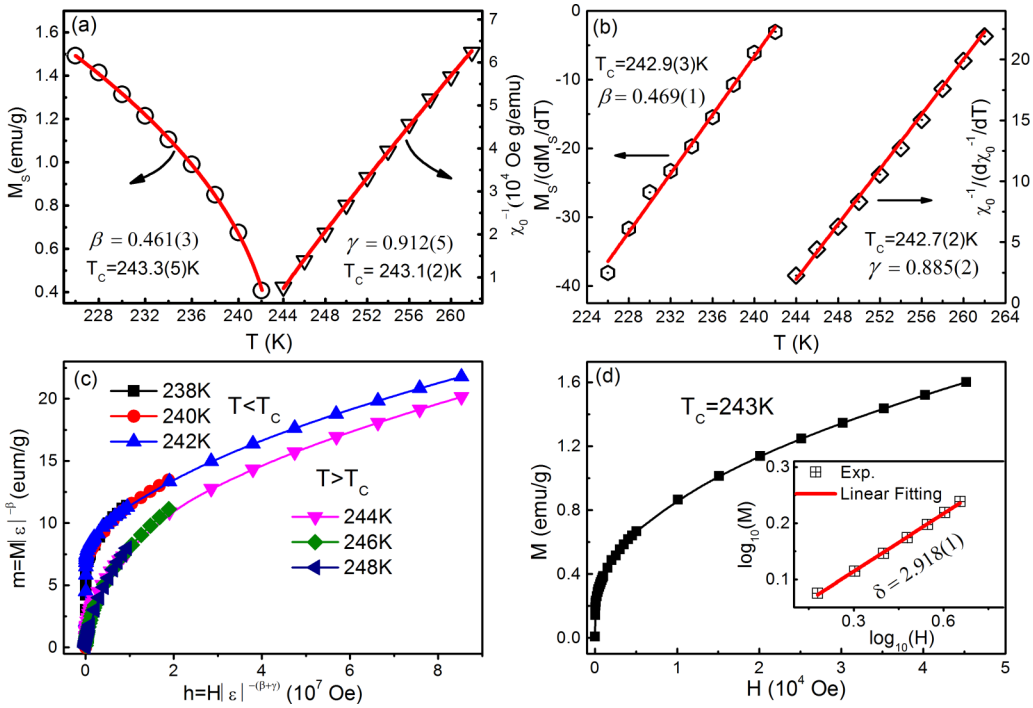

FIG. 4. (a) The temperature-dependent spontaneous magnetization M_S and inverse initial susceptibility χ_0^{-1} with the fitting solid curves. (b) KF plots for $M_S(T)$ and $\chi_0{}^{-1}(T)$. The solid lines are fitted. (c) Scaling plots around T_C using the values of β and γ determined by the KF method. (d) The critical isotherm analysis at T_C. The inset presents the plot on $\log_{10}$-$\log_{10}$ scale with a fitted solid line.

and δT^5 is the deviation term. The fitted values for γ, β, and δ are 29.3(1) mJ/mol K^2, 0.096(2) mJ/mol K^4, and $3.12(5)\times10^{-6}$ mJ/mol K^6, respectively. The Debye temperature $\Theta_D = (\frac{n\times1.94\times10^6}{\beta})^{1/3} = 466.1(3)$ K (where n is the number of atoms in a unit cell, and here it is 5) is derived from the value of parameter β for $AsNCr_3$ [28]. The aforementioned experimental parameters of magnetism, resistivity, and specific heat for $AsNCr_3$ are listed in Table II.

As we know, the Kadowaki-Woods ratio ($R_{KW} = A/\gamma^2$) and the Wilson ratio [$R_W = (\pi^2 k_B^2 \chi_0)/(3\mu_B^2\gamma)$] are the well-known measures of electron-electron correlation, where μ_B is Bohr magnon and k_B stands for Boltzmann constant [28]. Using the corresponding values (A, γ, and χ_0) listed in Table II, we can obtain the values of $0.493a_0$ [$a_0 = 1.0\times10^{-5}\,\mu\Omega\,\mathrm{cm/(mJ/mol\,K)^2}$] and 0.894 for R_{KW} and R_W, respectively. The value of R_{KW} here is smaller than the universal one of $a_0 = 1.0\times10^{-5}\,\mu\Omega\,\mathrm{cm/(mJ/mol\,K)^2}$ [34], suggesting a nonstrong correlated Fermi liquid behavior in the ground state of $AsNCr_3$. On the other hand, the value of $R_W = 0.894$ is smaller than the strong correlation limit of 2 according to the Anderson model [35], indicating a weak electron-electron correlation. Hereto, the basic physical properties of $AsNCr_3$ have been investigated, especially, there is a FM-PM transition around 243 K and an itinerant FM ground state. To further investigate the FM interaction, next we will perform the critical behavior analysis around FM-PM transition in $AsNCr_3$.

B. Critical behavior

It is well known that the critical behavior for a second-order magnetic phase transition is an efficient method to help us to understand the magnetic interaction of magnetic system [36,37]. Hereinbefore, a second-order FM-PM transition is observed in $AsNCr_3$. To further confirm it, we measured low-temperature (35–300 K) XRD for $AsNCr_3$ and did not observe structure phase transition around FM-PM transition as shown in Fig. S2 [33]. On the other hand, Fig. 3(a) displays the isothermal $M(H)$ curves in the vicinity of Curie temperature (T_C) and Fig. 3(b) shows the Arrott plots (M^2 vs H/M). According to the criterion suggested by Banerjee [38], the positive slopes in high fields correspond to a second-order magnetic transition [see Fig. 3(b)]. Usually, a second-order magnetic transition can be described by a series of critical exponents. In the vicinity of a second-order phase transition, the divergence of correlation length $\xi = \xi_0|(T_c - T)/T_c|^{-\nu}$ leads to universal scaling laws for the spontaneous magnetization (M_S) and initial susceptibility (χ_0). In this sense, the mathematical definitions of exponents obtained from $M(H)$ curves can be performed as follows [39]:

$$M_S(T) = M_0(-\varepsilon)^\beta, \quad \varepsilon < 0,\ T < T_c, \tag{4}$$

$$\chi_0(T)^{-1} = (h_0/M_0)\varepsilon^\gamma, \quad \varepsilon > 0,\ T > T_c, \tag{5}$$

$$M = DH^{1/\delta}, \quad \varepsilon = 0,\ T = T_c, \tag{6}$$

where $\varepsilon = (T - T_C)/T_C$ is the reduced temperature, h_0/M_0 and D are critical amplitudes. The parameters β, γ, and δ are the critical exponents, which are associated with M_S, χ_0, and T_C, respectively. The high-field parts of the Arrott plots [see Fig. 3(b)] are fitted with a linear function and then extrapolated to the $H/M = 0$ and $M^2 = 0$ axes to obtain M_S and χ_0, respectively. Using Eqs. (4) and (5), the β and γ are obtained as $\beta = 0.461(3)$ with $T_c = 243.3(5)$ K and

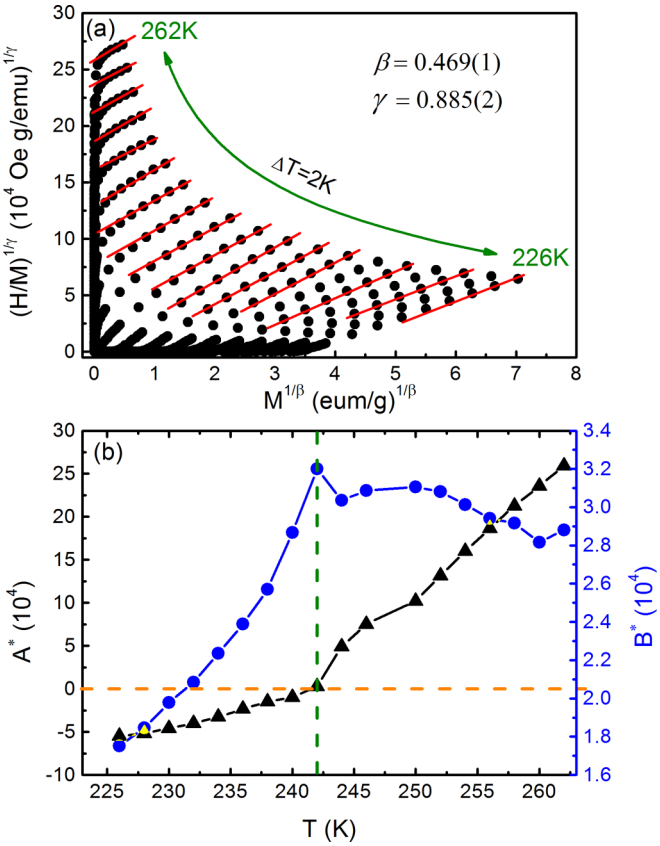

FIG. 5. (a) The $(H/M)^{1/\gamma}$ vs $M^{1/\beta}$ using the critical exponents obtained by the KF method. (b) Temperature-dependent modified coefficients A' and B'.

$\gamma = 0.912(5)$ with $T_c = 243.1(2)$ K, which can be seen in Fig. 4(a). The value of T_C obtained from the modified Arrott plot (MAP) is very close to that determined by the $dM(T)/dT$ curve.

In fact, the critical exponents can also be accurately determined by the Kouvel-Fisher (KF) method [40]:

$$M_S(T)/[dM_S(T)/dT] = (T - T_c)/\beta, \tag{7}$$

$$\chi_0{}^{-1}(T)/[d\chi_0{}^{-1}(T)/dT] = (T - T_c)/\gamma. \tag{8}$$

According to Eqs. (7) and (8), $M_S/(\mathrm{d}M_S/\mathrm{d}T)$ and $\chi_0^{-1}/(d\chi_0^{-1}/dT)$ vs T generate straight lines with slopes of $1/\beta$ and $1/\gamma$, respectively. The KF plots are displayed in Fig. 4(b). The estimated β and γ values are $\beta = 0.469(1)$ with $T_c = 242.9(3)$ K and $\gamma = 0.885(2)$ with $T_c = 242.7(3)$ K, which are basically consistent with those derived from the MAP method. According to the prediction of the scaling equation, in the asymptotic critical region, the magnetic equation is written as follows [41]:

$$M(H,\varepsilon) = \varepsilon^{\beta} f_{\pm}(H/\varepsilon^{\beta+\gamma}), \tag{9}$$

where $f_{\pm}$ are regular functions with f_+ for $T > T_C$ and f_- for $T < T_C$. This means that the renormalized magnetization $m \equiv \varepsilon^{-\beta} M(H,\varepsilon)$ vs the renormalized field $h \equiv H\varepsilon^{-(\beta+\gamma)}$. Namely, $m = f_{\pm}(h)$ forms two universal curves for $T > T_C$ and $T < T_C$, respectively. Based on this scaling equation, $m(h)$ curves around T_c are plotted in Fig. 4(c), where all the magnetization data collapse onto two universal curves. The obedience of the scaling equation over the entire range of the normalized variables indicates the reliability of the obtained critical exponents.

According to Eq. (6), the third critical exponent δ can be determined from a critical isotherm (CI) $M(H)$ curve analysis. Figure 4(d) displays $M(H)$ curve at $T_C = 243$ K and the inset shows the plots on the $\log_{10}$-$\log_{10}$ scale. The $\log_{10}(M)$-$\log_{10}(H)$ relation yields a straight line with the slope $1/\delta$ at high magnetic field, which determines $\delta = 2.918(1)$. In addition, all these critical exponents (γ, β, and δ) fulfill the Widom scaling relation ($\delta = 1 + \gamma/\beta$) according to statistical theory [42]. Given the β and γ values from the MAP method and the KF method, the values of δ can be estimated as 2.978(2) and 2.887(3), respectively. These values of δ are close to that obtained from the CI analysis, indicating the obtained critical exponents are reliable.

According to the Arrott-Noakes equation of state, H/M vs M follows $(H/M)^{1/\gamma} = (T - T_C)/T_C + (M/M_1)^{1/\beta}$, where M_1 is a constant [43]. However, the Arrott-Noakes equation of state is strictly obeyed only at the limit of T approaching to T_C. More universally, H/M vs M obeys

$$(H/M)^{1/\gamma} = A' + B'M^{1/\beta}, \tag{10}$$

where A' and B' are temperature-dependent coefficients [44]. Consequently, the experimental data are reconstructed as $(H/M)^{1/\gamma}$ vs $M^{1/\beta}$ using the critical exponents obtained by the KF method as shown in Fig. 5(a). Obviously, all lines are parallel to each other and the lines around T_C pass through the origin. At the same time, the obtained A' and B' are displayed in Fig. 5(b). One can see that A' just passes the origin around T_C and the maximum of B' locates at T_C. All the above-mentioned

TABLE III. Comparison of the critical exponents of $AsNCr_3$ with different theoretical models. MAP, KF, and CI stand for modified Arrott plot, Kouvel-Fisher method, and critical isotherm analysis, respectively.

Composition	Ref.	T_C(K)	β	γ	δ
$AsNCr_3$ (MAP)	This work	243.3(5)	0.461(3)	0.912(5)	2.978(2)
$AsNCr_3$ (KF)	This work	242.9(3)	0.469(1)	0.885(2)	2.887(3)
$AsNCr_3$ (CI)	This work	243			2.918(2)
Tricritical mean field	[43]		0.25	1.0	5.0
Mean-field model	[43]		0.5	1.0	3.0
3D Heisenberg model	[43]		0.365	1.386	4.8
3D Ising model	[43]		0.325	1.24	4.82

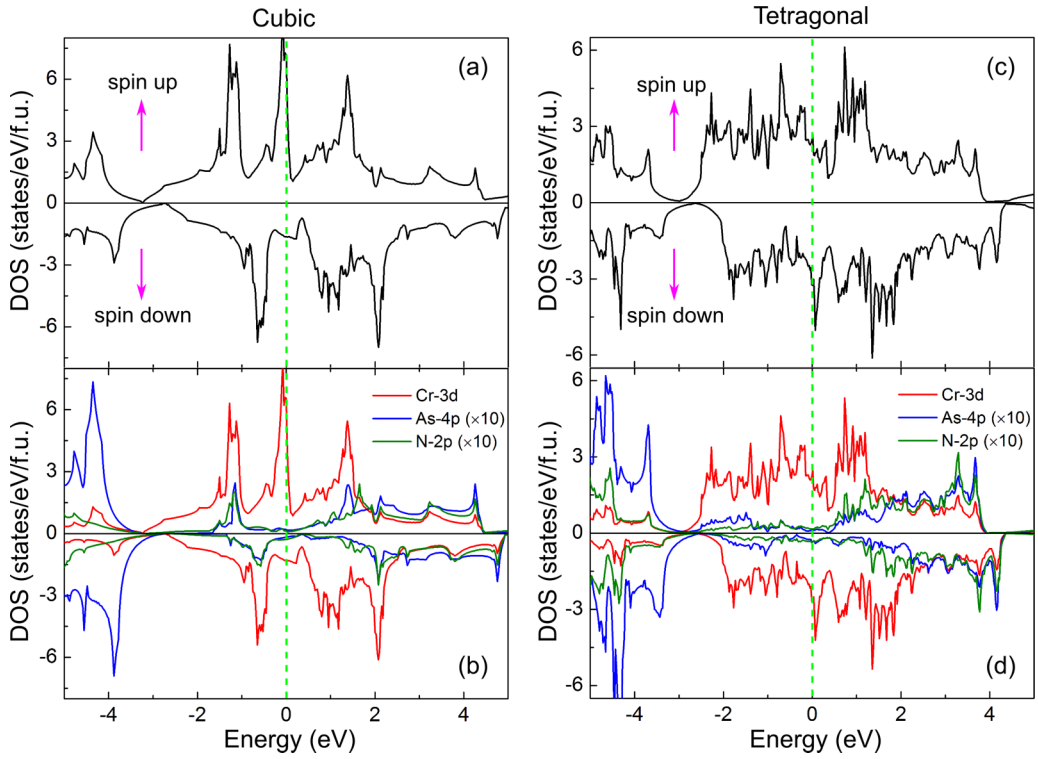

FIG. 6. (a) Total and (b) atom-orbital-projected density of states of $AsNCr_3$ with cubic-antiperovskite structure (Pm-$3m$); (c) Total and (d) atom-orbital-projected DOS of $AsNCr_3$ with tetragonal-antiperovskite structure ($I4/mcm$). The positive and negative values represent the DOS of up and down spins, respectively. The Fermi level is set to be 0 eV.

results suggest that our obtained critical exponents are reliable and intrinsic. The obtained critical exponents of $AsNCr_3$ by different methods, as well as those from different theoretical models, are listed in Table III for comparison. It is found that our obtained γ, β, and δ are quite close to the values of the mean-field model, indicating that the FM coupling in $AsNCr_3$ is a long-range interaction.

Besides, the universality class of the magnetic phase transition mainly depends on the exchange interaction $J(r)$ for a homogeneous magnet [44]. A renormalization group theory analysis suggests a long-range attractive interactions decay as $J(r) \sim r^{-(d+\sigma)}$, where d and σ are the spatial dimension and a constant, respectively [45]. For the long-range interaction, σ can be determined by the following equation [44–46]:

$$\gamma = 1 + \frac{4(n+2)}{d(n+8)}\Delta\sigma + \frac{8(n+2)(n-4)}{d^2(n+8)^2} \times \left[1 + \frac{2G(d/2)(7n+20)}{(n-4)(n+8)}\right]\Delta\sigma^2, \quad (11)$$

where $\Delta\sigma = (\sigma - d/2)$ and $G(d/2) = 3 - (d/2)^2/4$, n is the spin dimensionality. For a three-dimensional system, $d = 3$, and there is a relation $J(r) \sim r^{-(3+\sigma)}$. When $\sigma \geqslant 2$, the three-dimension Heisenberg model ($\beta = 0.365$, $\gamma = 1.386$, and $\delta = 4.8$) is valid and $J(r)$ decreases faster than r^{-5}. For $\sigma \leqslant 3/2$, the mean-field model ($\beta = 0.5$, $\gamma = 1.0$, and $\delta = 3.0$) is satisfied, where $J(r)$ decreases slower than $r^{-4.5}$ [44]. According to Eq. (11), the value of σ for $AsNCr_3$ is about $1.319(2) \leqslant 3/2$, confirming the long-range magnetic coupling.

C. First-principles calculations

To investigate the origin of the long-range magnetic ordering in our system, we carried out first-principles calculations for the tetragonal $AsNCr_3$ and, for comparison, the results of the cubic structure are also shown. The occurrence of the magnetic ordering can be firstly evaluated by the Stoner criterion, which is expressed as $N(E_F)\times I > 1$, where $N(E_F)$ denotes the number of DOS at the Fermi level in the nonmagnetic state. I is the Stoner exchange parameter and can be estimated based on the relation $\Delta E_{ex} = m \times I$, where ΔE_{ex} and m are the exchange splitting energy and magnetic moment, respectively [47]. The ΔE_{ex} between the spin-up and spin-down bands are estimated from the total DOS shown in Figs. 6(a) and 6(c) for cubic and tetragonal $AsNCr_3$, respectively. Here we only consider a collinear ferromagnetic configuration where the spins of all the Cr atoms are parallel to each other. All the parameters for the Stoner criterion are listed in Table IV. We can see that the Stoner criterion is satisfied for both the cubic and tetragonal symmetries and thus the ferromagnetism arises in both of the two structures.

TABLE IV. Calculated $N(E_F)$, ΔE_{ex}, m, I, and $N(E_F)\times I$ for cubic and tetragonal-antiperovskite structures.

Symmetry	$N(E_F)$ (states/eV/spin)	ΔE_{ex} (eV)	m (μ_B/f.u.)	I (eV)	$N(E_F) \times I$
Cubic	4.18	0.70	2.46	0.28	1.17
Tetragonal	2.93	0.80	2.31	0.35	1.03

It is well known that for most of the antiperovskite compounds AXM_3 with a cubic symmetry, there is a strong hybridization of M-3d and X-2p states in M_6X octahedra [17,44,48]. To further investigate the origin of the magnetic ordering, we show in Figs. 6(b) and 6(d) the partial DOS. We can see that for both structures, the DOS near the Fermi level is dominated by the Cr-3d states, which is the same as in the other AXM_3 systems [49]. However, in $AsNCr_3$, besides a strong hybridization between Cr-3d and N-2p states, we also observe a strong hybridization between Cr-3d and As-4p states near the Fermi level, for both the cubic and tetragonal structures. The difference between the two structures is that the tetragonal one has a much wider bandwidth in the vicinity of the Fermi level. Therefore, the Cr-3d electrons are much more itinerant in the tetragonal $AsNCr_3$, giving rise to the itinerant magnetism. In fact, the itinerant ferromagnetism of $AsNCr_3$ is also confirmed by the Rhodes-Wolfarth ratio as discussed above. Thus, the strong hybridization between Cr-3d and N-2p states as well as between Cr-3d and As-4p states may be an important factor to result in the long-range $J(r)$ in our system.

IV. CONCLUSIONS

In summary, the synthesis, structure, and magnetic and electrical/thermal transport properties of tetragonal-antiperovskite $AsNCr_3$ have been investigated systematically. A second-order FM-PM transition at 243 K was observed, where the resistivity curve exhibits a kink and the specific heat also shows a peak. The metallic behavior over the whole measured temperature range (2–300 K) and low-temperature Fermi liquid behavior were suggested by the resistivity curve of $AsNCr_3$. Given the experimental parameters of magnetism, resistivity, low-temperature specific heat, the weak electron-electron correlation were confirmed by both the $R_{KW} = 0.493a_0 < a_0[a_0 = 1.0\times10^{-5}\,\mu\Omega\,\mathrm{cm/(mJ/mol\,K)^2}]$ and $R_W = 0.894 < 2$. The value of $RWR = 1.312 > 1$ indicates an itinerant ferromagnetism in $AsNCr_3$. Consistently, critical exponents obtained by using different methods [MAP: $\beta = 0.461(3)$, $\gamma = 0.912(5)$, and $\delta = 2.978(2)$; KF: $\beta = 0.469(1)$, $\gamma = 0.885(2)$, and $\delta = 2.887(3)$; CI: $\delta = 2.918(2)$] are very close to the theoretical values of the mean-field model ($\beta = 0.5$, $\gamma = 1.0$, and $\delta = 3.0$), indicating the existence of a long-range FM interaction in $AsNCr_3$. Furthermore, the obtained exchange interaction distance $J(r) \sim r^{-4.3}$ decreases more slowly than the value of mean-field model [$J(r) \sim r^{-4.5}$], further confirming the long-range FM coupling in our system. The strong hybridization between Cr-3d and N-2p states as well as between Cr-3d and As-4p states may be responsible for the long-range itinerant ferromagnetism in tetragonal-antiperovskite $AsNCr_3$.

ACKNOWLEDGMENTS

This work was supported by the National Natural Science Foundation of China under Contracts No. U1632158 and No. 51322105, Natural Science Foundation of Anhui Province (Grants No. 1608085QE107 and No. 1708085QA18), and Key Research Program of Frontier Sciences, CAS (Grant No. QYZDB-SSW-SLH015). This work was also supported by the Youth Innovation Promotion Association of CAS (Grant No. 2014283).

S.L. and H.L. contributed equally to this work.

[1] T. He, Q. Huang, A. P. Ramirez, Y. Wang, K. A. Regan, N. Rogado, M. A. Hayward, M. K. Haas, J. S. Slusky, K. Inumara, H. W. Zandbergen, N. P. Ong, and R. J. Cava, Nature (London) **411**, 54 (2001).

[2] E. O. Chi, W. S. Kim, and N. H. Hur, Solid State Commun. **120**, 307 (2001).

[3] L. Ding, C. Wang, L. H. Chu, J. Yan, Y. Y. Na, Q. Z. Huang, and X. L. Chen, Appl. Phys. Lett. **99**, 251905 (2011).

[4] S. Lin, B. S. Wang, J. C. Lin, Y. N. Huang, W. J. Lu, B. C. Zhao, P. Tong, W. H. Song, and Y. P. Sun, Appl. Phys. Lett. **101**, 011908 (2012).

[5] B. S. Wang, P. Tong, Y. P. Sun, L. J. Li, W. Tang, W. J. Lu, X. B. Zhu, Z. R. Yang, and W. H. Song, Appl. Phys. Lett. **95**, 222509 (2009).

[6] K. Kamishima, T. Goto, H. Nakagawa, N. Miura, M. Ohashi, N. Mori, T. Sasaki, and T. Kanomata, Phys. Rev. B **63**, 024426 (2000).

[7] D. Matsunami, A. Fujita, K. Takenaka, and M. Kano, Nat. Mater. **14**, 73 (2015).

[8] Y. Sun, C. Wang, Q. Z. Huang, Y. F. Guo, L. H. Chu, M. Arai, and K. Yamaura, Inorg. Chem. **51**, 7232 (2012).

[9] K. Takenaka and H. Takagi, Appl. Phys. Lett. **87**, 261902 (2005).

[10] J. Yan, Y. Sun, H. Wu, Q. Z. Huang, C. Wang, Z. X. Shi, S. H. Deng, K. W. Shi, H. Q. Lu, and L. H. Chu, Acta Mater. **74**, 58 (2014).

[11] B. Song, J. K. Jian, H. Q. Bao, M. Lei, H. Li, G. Wang, Y. P. Xu, and X. L. Chen, Appl. Phys. Lett. **92**, 192511 (2008).

[12] B. S. Wang, P. Tong, Y. P. Sun, X. B. Zhu, Z. R. Yang, W. H. Song, and J. M. Dai, Appl. Phys. Lett. **97**, 042508 (2010).

[13] X. H. Zhang, Q. Yuan, J. C. Han, J. G. Zhao, J. K. Jian, Z. H. Zhang, and B. Song, Appl. Phys. Lett. **103**, 022405 (2013).

[14] S. Dhar, O. Brandt, A. Trampert, K. J. Friedland, Y. J. Sun, and K. H. Ploog, Phys. Rev. B **67**, 165205 (2003).

[15] K. Asano, K. Koyama, and K. Takenaka, Appl. Phys. Lett. **92**, 161909 (2008).

[16] Ph. L'Héritier, D. Fruchart, R. Madar, and R. Fruchart, in *1.5.6.2 Crystallographic Properties of M{c}XM{f}{3} Compounds*, edited by H. P. J. Wijn, Landolt-Börnstein–Group III Condensed Matter 19C (Alloys and Compounds of d-Elements with Main Group Elements. Part 2), SpringerMaterials (Springer-Verlag, Berlin, Heidelberg, 1988), doi:10.1007/10353201_69.

[17] X. C. Kan, B. S. Wang, L. Zhang, L. Zu, S. Lin, J. C. Lin, P. Tong, W. H. Song, and Y. P. Sun, Phys. Chem. Chem. Phys. **19**, 13703 (2017).

[18] X. C. Kan, B. S. Wang, L. Zu, S. Lin, J. C. Lin, P. Tong, W. H. Song, and Y. P. Sun, RSC Adv. **6**, 104433 (2016).

[19] J. C. Lin, P. Tong, D. P. Cui, C. Yang, J. Yang, S. Lin, B. S. Wang, W. Tong, L. Zhang, Y. M. Zou, and Y. P. Sun, Sci. Rep. **5**, 7933 (2015).

[20] T. Shimizu, T. Shibayama, K. Asano, and K. Takenaka, J. Appl. Phys. **111**, 07A903 (2012).

[21] L. Zu, S. Lin, Y. Liu, J. C. Lin, B. Yuan, X. C. Kan, P. Tong, W. H. Song, and Y. P. Sun, Appl. Phys. Lett. **108**, 031906 (2016).
[22] H. Boller, Monatsh. Chem. **99**, 2444 (1968).
[23] H. Nowotny, Angew. Chem. Int. Ed. **11**, 906 (1972).
[24] T. Waki, K. Takao, Y. Tabata, H. Ohta, T. Yajima, Z. Hiroi, and H. Nakamura, J. Phys. Soc. Jpn. **86**, 104706 (2017).
[25] G. Kresse and J. Furthmüller, Phys. Rev. B **54**, 11169 (1996).
[26] G. Kresse and D. Joubert, Phys. Rev. B **59**, 1758 (1999).
[27] Z. Liu, T. Waki, Y. Tabata, and H. Nakamura, Phys. Rev. B **89**, 054435 (2014).
[28] P. Tong, Y. P. Sun, X. B. Zhu, and W. H. Song, Phys. Rev. B **73**, 245106 (2006).
[29] X. Lin, V. Taufour, S. L. Bud'ko, and P. C. Canfield, Phys. Rev. B **88**, 094405 (2013).
[30] P. Rhodes and E. P. Wohlfarth, Proc. R. Soc. London Ser. A **273**, 247 (1963).
[31] T. H. Scabarozi, S. Amini, P. Finkel, O. D. Leaffer, J. E. Spanier, M. W. Barsoum, M. Drulis, H. Drulis, W. M. Tambussi, J. D. Hettinger, and S. E. Lofland, J. Appl. Phys. **104**, 033502 (2008).
[32] R. J. Goetsch, V. K. Anand, A. Pandey, and D. C. Johnston, Phys. Rev. B **85**, 054517 (2012).
[33] See Supplemental Material at http://link.aps.org/supplemental/10.1103/PhysRevB.98.014412 for the DSC curve between 300 and 230 K (Fig. S1) and the low-temperature (35–300 K) XRD results (Fig. S2) for $AsNCr_3$.
[34] K. Kadowaki and S. B. Woods, Solid State Commun. **58**, 507 (1986).
[35] K. G. Wilson, Rev. Mod. Phys. **47**, 773 (1975).
[36] J. Y. Fan, L. S. Ling, B. Hong, L. Zhang, L. Pi, and Y. H. Zhang, Phys. Rev. B **81**, 144426 (2010).
[37] K. Ghosh, C. J. Lobb, R. L. Greene, S. G. Karabashev, D. A. Shulyatev, A. A. Arsenov, and Y. Mukovskii, Phys. Rev. Lett. **81**, 4740 (1998).
[38] B. K. Banerjee, Phys. Lett. **12**, 16 (1964).
[39] M. E. Fisher, Rep. Prog. Phys. **30**, 615 (1967).
[40] J. S. Kouvel and M. E. Fisher, Phys. Rev. **136**, A1626 (1964).
[41] H. E. Stanley, *Introduction to Phase Transitions and Critical Phenomena* (Oxford University Press, London, 1971).
[42] L. P. Kadanoff, Physics **2**, 263 (1966).
[43] A. Arrott and J. E. Noakes, Phys. Rev. Lett. **19**, 786 (1967).
[44] L. Zhang, B. Wang, Y. Sun, P. Tong, J. Fan, C. Zhang, L. Pi, and Y. Zhang, Phys. Rev. B **85**, 104419 (2012).
[45] M. E. Fisher, S. Ma, and B. G. Nickel, Phys. Rev. Lett. **29**, 917 (1972).
[46] S. F. Fischer, S. N. Kaul, and H. Kronmüller, Phys. Rev. B **65**, 064443 (2002).
[47] H. Rosner, R. Weht, M. D. Johannes, W. E. Pickett, and E. Tosatti, Phys. Rev. Lett. **88**, 027001 (2001).
[48] F. Grandjean and A. Gerard, J. Phys. F: Metal Phys. **6**, 451 (1976).
[49] K. Motizuki and H. Nagai, J. Phys. C **21**, 5251 (1988).